Polycrystalline modeling of the behavior of neutron-irradiated recrystallized zirconium alloys during strain path change tests

F. Onimus, M. Bono, B. Verhaeghe, A. Soniak, P. Pilvin

Polycrystalline modeling of the behavior of neutron-irradiated recrystallized zirconium alloys during strain path change tests

Authors: *F. Onimus[1*], M. Bono[2], B. Verhaeghe[2], A. Soniak[3], P. Pilvin[4]*

[1]CEA, Section for Applied Metallurgy Research, 91191 Gif-Sur-Yvette, Cedex, France,

[2]CEA, Section for Study of Irradiated Materials, 91191 Gif-Sur-Yvette, Cedex, France,

[3]CEA, Nuclear Energy Division, 91191 Gif-Sur-Yvette, Cedex, France,

[4]Institut de Recherche Dupuy de Lôme, Université de Bretagne Sud, UMR-CNRS 6027, rue St Mandé, 56321 Lorient, France

** corresponding author : fabien.onimus@cea.fr*

Keywords:

dislocations, cyclic loading, polycrystalline material, mechanical testing

Highlights:

- Cyclic strain softening occurs in neutron irradiated recrystallized zirconium alloys when subjected to cyclic loading
- The cyclic strain softening is due to the clearing of irradiation defects by gliding dislocations
- The more rapid cyclic strain softening observed during internal pressure test is explained by the easier clearing of loops by dislocations gliding in the basal plane.
- The polycrystalline model developed reproduces correctly this complex behavior

Abstract:

During normal operating conditions, zirconium alloy nuclear fuel cladding tubes experience various biaxial loadings with complex strain path histories. Experiments have been conducted on neutron-irradiated thin cladding tubes in order to study the response to changes in the loading path. These tests consist of alternate internal pressure tests and axial tensile tests. During the internal pressure test steps, the flow stress exhibits significant cyclic strain softening, while axial tensile tests exhibit a smaller degree of cyclic strain softening. TEM analyses of the tested samples have revealed that the observed mechanical behavior can be attributed to clearing of irradiation-induced defect by gliding dislocations. The cyclic strain softening observed for internal pressure tests is due to clearing of defect by dislocations gliding in the basal planes. The smaller degree of cyclic strain softening in tensile tests is due to clearing of defects by dislocations gliding in the prismatic and pyramidal planes. A polycrystalline model has been developed to simulate these tests. This model is able to reproduce many features of the complex behavior of the material and provides a better understanding of the role of the clearing of defects and the contribution of kinematic hardening on the behavior of neutron-irradiated recrystallized zirconium alloys.

Introduction

Zirconium alloys are used in the nuclear industry as fuel rod cladding in pressurized water reactors. Since the cladding is the first confinement barrier against the dissemination of radioactive species, it is of prime importance to guarantee its mechanical integrity throughout its lifetime.

During normal operating conditions, the cladding experiences various biaxial loadings with complex strain path histories. Furthermore, during severe power transients, the applied stress on the clad can be significant, leading to irreversible plastic deformation. In order to adequately predict the stress and strain states in the clad and then to guarantee its mechanical integrity, a good knowledge of the response of irradiated zirconium alloys to strain path changes is required.

In the open literature, very few articles report results concerning changes of loading path tests conducted on neutron-irradiated zirconium specimens. Researchers (O'Donnell and Langer, 1964) (Wisner et al., 1994) have conducted cyclic tension-compression tests on specimens taken along the transverse direction of a thick sheet. However, it is difficult to perform this type of test on thin cladding tubes. In order to study the response of thin cladding tubes to changes in the loading path, non-standard tests have been proposed (Onimus et al., 2018). These tests are not representative of loading that may occur inside the reactor, where creep, stress relaxation and even irradiation creep occur. Instead, these tests are intended to evaluate how thin cladding tubes reacts to significant changes in loading path, in relationship with the deformation mechanisms.

Several authors (O'Donnell and Langer, 1964) (Wisner et al., 1994) (Onimus et al., 2018) (MacEwen et al., 1981) (Christodoulou, 1989) (Kassam and Wang ,1993) (Delobelle et al., 1996) (Li et al., 2003) have performed cyclic tests and tests with changes in loading path on non-irradiated zirconium alloys. These tests have been able to show the well-known anisotropic behavior of zirconium alloys, but they have also revealed the complex strain hardening behavior of these materials. The multiaxial strain hardening behavior of metals is often analyzed and modeled (Miller, 1987) (Lemaitre and Chaboche, 1990) (Chaboche, 1989) (Chaboche, 2008) using the concept of a yield surface. In this framework, strain hardening is the result of the expansion of the yield surface, which is called "isotropic" hardening, and the translation of the yield surface, which is referred to as "kinematic" hardening. One common example of kinematic hardening is the Bauschinger effect during cyclic tension-compression tests, where a test conducted in tension can lead to a reduced yield stress in subsequent compression, when compared to the yield stress measured in compression without previous tension. Within this framework, it is convenient to define two quantities: the kinematic stress tensor ($\boldsymbol{X}$), which is associated to the translation of the yield surface, and the isotropic stress (R), a scalar quantity, which is associated to the size of the yield surface (Chaboche, 1989). The evolution of a Von Mises yield surface during an axial tensile test is represented schematically on Figure 1 assuming a) only isotropic

hardening (increase of the size of the yield surface) or b) only kinematic hardening (translation of the yield surface).

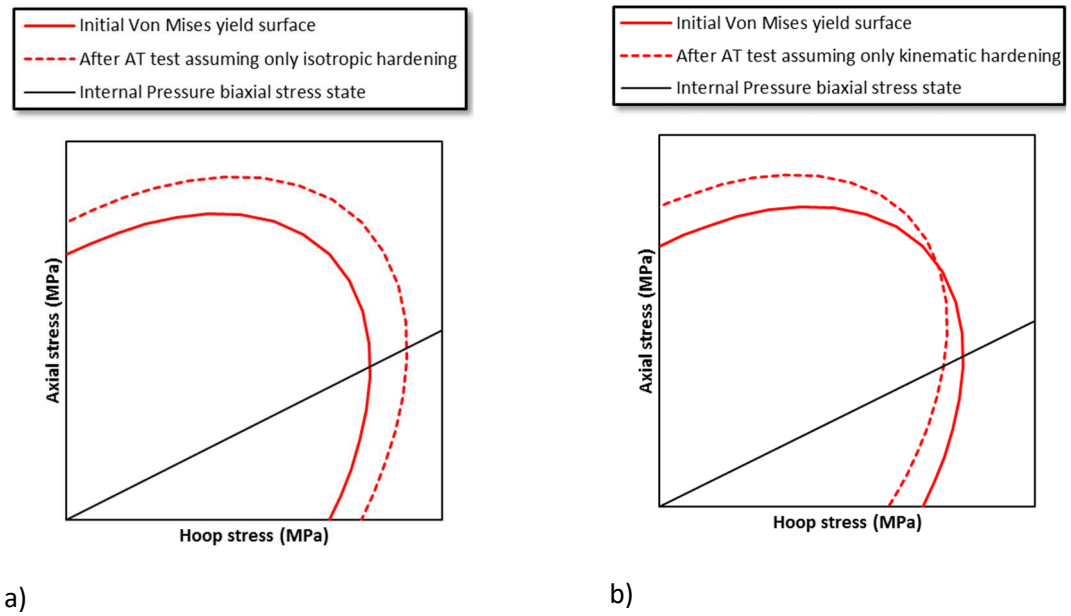

a) b)

Figure 1: Schematic of the evolution of a Von Mises yield surface during an axial tensile test assuming: a) only isotropic hardening, b) only kinematic hardening.

In the case of non-irradiated recrystallized zirconium alloys, it has been demonstrated, mainly by using tension-compression tests on thick tubes or thick specimens, that the Bauschinger effect is strong (MacEwen et al., 1981) (Christodoulou, 1989) (Kassam and Wang ,1993) (Delobelle et al., 1996) (Li et al., 2003), thus proving that the kinematic hardening is significant. On the other hand, only limited isotropic hardening has been reported (Li et al., 2003) (Onimus et al., 2006). The role of the kinematic hardening on the creep behavior of zirconium alloys has also been demonstrated (Sedláček and Deuble, 2016).

Concerning neutron-irradiated recrystallized zirconium alloys, O'Donnell and Langer (O'Donnell and Langer, 1964) and Wisner et al. (Wisner et al., 1994) have shown that a striking phenomenon occurs during cyclic tension-compression tests. In contrast to non-irradiated recrystallized zirconium alloys, which exhibit cyclic strain hardening, neutron-irradiated recrystallized zirconium alloys exhibit cyclic strain softening. Furthermore, by analyzing the stabilized hysteresis loops, Wisner et al. (Wisner et al., 1994) have shown that the irradiated material exhibits a Bauschinger effect, proving that kinematic hardening also occurs after irradiation. Except for these results, very few is known concerning the influence of change of loading path on the behavior of neutron irradiated zirconium alloys. Furthermore, there is yet no physically based model able to reproduce the behavior of this materials in these conditions.

More generally, cyclic mechanical behavior hexagonal close-packed (hcp) metals and alloys has always been an important field of research for fatigue or forming issues. Recently, improvements have been made to model and simulate the influence of changes in strain-path on the behavior of various hcp metals, often involving both dislocation glide and twinning (Capolungo et al., 2009; Proust et al., 2009; Knezevic et al., 2013).

Concerning the modeling of irradiated alloys for nuclear applications, several authors have recently proposed various approaches to account for the presence of irradiation defects using crystal plasticity modeling (Barton et al., 2013; Xiao et al, 2015; Xiao et al., 2016; Hure et al., 2016; Chakraborty and Biner, 2016). In the case of irradiated zirconium alloys, there has been only few attempt to take into account irradiation effects into a crystal plasticity framework (Onimus and Béchade, 2009; Erinosho and Dunne, 2015).

This paper describes non-standard mechanical tests involving changes of strain path, conducted on neutron-irradiated thin tubes made of a recrystallized zirconium alloy. The material and the testing machine are first described, and then the results are presented and analyzed. Transmission Electron Microscopy observations of the microstructure after testing are discussed in light of the observed mechanical behavior. A physically based polycrystalline model (Onimus and Béchade, 2009) (Onimus et al., 2012) is improved to describe the observed behavior. Numerical simulations are then compared to the experimental results.

Experimental details

Material studied and irradiation conditions

Two specimens made of a Zr1%Nb recrystallized zirconium alloy have been used for this study. The chemical composition of the alloy is given in Table 1.

Table 1 : Chemical composition of the recrystallized Zr1%Nb cladding tubes (wt %).

Alloy	Sn	Fe	Cr	Nb	O
Zr1%Nb	<0.003	0.037	0.0049	1.0	0.14

The alloy exhibits equiaxed grains with a typical grain size of 6 µm. The texture of the material is also typical of recrystallized zirconium alloys in the form of thin cold rolled tubes. The maximum density for the $\{0002\}$ poles, of the hexagonal close-packed (h.c.p) crystalline grains, are in the hoop (or Transverse Direction, TD) – radial (or Normal Direction, ND) plane with the maximum pole density

tilted at 30° to the radial direction (Figure 1b), one of the $\{11\bar{2}0\}$ pole of the crystal being along the axial direction (or Rolling Direction, RD).

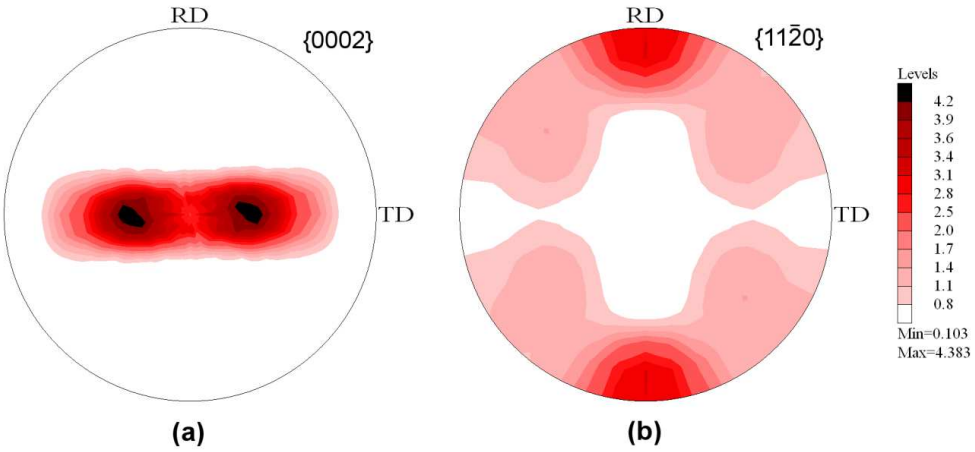

Figure 2: a) {0002} pole figure and b) $\{11\bar{2}0\}$ pole figure of a recrystallized Zr1%Nb alloy thin tube. TD refers to the transverse or hoop direction and RD refers to the rolling or axial direction of the tube. A level value equal to one corresponds to the isotropic texture.

The two samples were taken from a fuel rod irradiated in a nuclear power plant up to 5 PWR cycles (corresponding to a burn up of 61 GWd/t and to a neutron fluence of approximately 12×10^{25} n/m^2 (E > 1 MeV)) at a temperature of approximately 350°C.

Mechanical testing machine, mechanical tests and sample geometry

The mechanical testing machine is installed in a hot cell and is able to load a tubular sample with a tensile force and an internal pressure via pressurized oil. Thus, biaxial mechanical loading can be achieved where both an axial stress (σ_{zz}) and a hoop stress ($\sigma_{\theta\theta}$) can be applied simultaneously or successively on the same sample. For these tests, it is convenient to define a biaxiality ratio (α) as: $\alpha = \sigma_{zz}/\sigma_{\theta\theta}$. In order to study the effect of a change in the loading path, we have performed alternate loading and unloading steps with a biaxiality ratio of $\alpha = \sigma_{zz}/\sigma_{\theta\theta}$=0.47, corresponding to a simple internal pressure test (IP) without additional external axial force. They are followed by loading-unloading steps corresponding to simple axial tensile test (AT). In this case, the biaxiality ratio should be infinite, but because of a software constraint, a biaxiality ratio of $\alpha = \sigma_{zz}/\sigma_{\theta\theta}$=100 was adopted. The experiment conducted on one of the irradiated samples, referred to as IP-AT, consists of an internal pressure (IP) loading-unloading step followed by an axial tensile (AT) loading-unloading step, this sequence being repeated six times. The total strain increment in the hoop direction for each internal pressure step is 0.5%. The total strain increment in the axial direction for each axial tensile step is 1%. The second experiment, referred to as AT-IP, consists of an axial tensile loading-unloading

step, followed by an internal pressure (IP) loading-unloading step. Once again, the sequence is repeated six times. The total strain increment in the axial direction for each axial tensile step is also 1%, but the total hoop strain increment for each internal pressure step is 0.6%. The mechanical tests were conducted at 350°C. The applied strain rate was constant and equal to 3×10^{-4} s^{-1} in the hoop direction for the internal pressure tests and 3×10^{-4} s^{-1} in the axial direction for the axial tensile tests. The details concerning the mechanical tests are listed in Table 2.

The tubular samples had an external diameter of 9.5 mm, thickness of 0.57 mm, and length of 90 mm. The axial force is applied to the tube using a servo-hydraulic actuator. The machine uses silicone-based oil in a hydraulic cylinder to apply an internal pressure of up to 2000 bar to the sample. Testing can be performed at temperatures of up to 400 °C.

Four radial extensometers, which are grouped into two diametrically opposed pairs, are mounted every 90° around the sample and measure the hoop strain throughout the test. Each extensometer consists of a ceramic rod that passes through the wall of the furnace to contact the sample inside the furnace. The opposite end of the ceramic rod is connected to an LVDT sensor outside the furnace that measures the linear displacement of the rod. The four rods are positioned so that they contact and measure the sample at its mid-plane. The change in external diameter is measured at 350°C during the test and the initial diameter is measured at room temperature. The thickness of the tube is also measured at room temperature.

The axial strain of the sample is measured using an extensometer that consists of two ceramic rods that contact the sample inside the furnace. The gauge length of the axial extensometer is 25 mm and is accurately measured at 350°C. A capacitance probe outside the furnace measures the displacement of the rods to determine the sample strain.

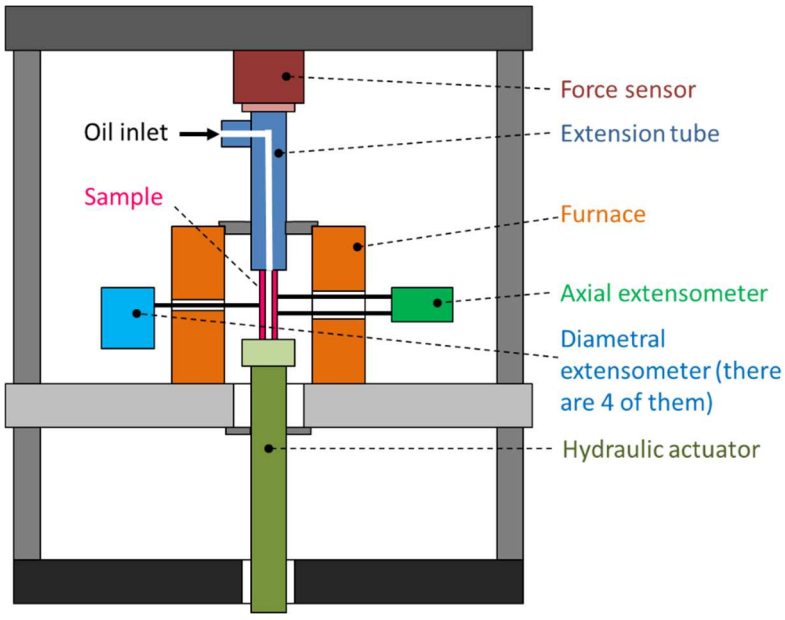

Figure 3: Schematic of the biaxial testing machine installed in a hot cell.

Table 2: Mechanical tests performed on neutron-irradiated Zr1%Nb samples.

	IP-AT		AT-IP	
Step	Biaxiality ratio	Total strain increment	Biaxiality ratio	Total strain increment
1	α=0.47	0.5%	α=100	1%
2	α=100	1%	α=0.47	0.6%
3	α=0.47	0.5%	α=100	1%
.	.	.	.	.
.	.	.	.	.
.	.	.	.	.
10	α=100	1%	α=0.47	0.6%
11	α=0.47	0.5%	α=100	1%
12	α=100	1%	α=0.47	0.6%

The formulas used to analyze the mechanical tests have been detailed in (Onimus et al., 2018) and are recalled in Appendix. All the stress and strain values given here are true stresses and true strains. The plastic strain tensor components are computed by substracting the elastic deformation to the total deformation. In the following, the true stress is plotted as a function of the true plastic strain.

Moreover, in order to have a better understanding of the effect of the cumulated plastic strain on the behavior of the material, an equivalent cumulated plastic strain has been computed. Furthermore, in order to compare the tests with each other, the stress –plastic strain curves have been translated so that the beginning of each step of the test starts with zero equivalent plastic strain. This is referred to as the translated equivalent plastic strain.

During the experiments, it has been observed that the hoop extensometers that were used for these tests did not correctly measure the reduction in diameter during the axial tensile tests. Therefore, the equivalent cumulated plastic strain assuming an isotropic behavior has been computed rather than the anisotropic experimental equivalent cumulated plastic strain. During each axial tensile test, the increment in equivalent plastic strain is thus given by equation 1. For each internal pressure test, it is given by equation 2. The equivalent cumulated plastic strain is then computed by adding the equivalent plastic strain increment for each step. This computation is done in exactly the same way to analyze the experiments and the numerical simulations described in the last section of this article.

$$\Delta\varepsilon_{eq}^{p} = \Delta\varepsilon_{zz}^{p} \quad (1)$$

$$\Delta\varepsilon_{eq}^{p} = \frac{2}{\sqrt{3}}\Delta\varepsilon_{\theta\theta}^{p} \quad (2)$$

Furthermore, with this equivalent plastic strain computed for isotropic behavior, it is possible to evaluate the flow stress for an equivalent plastic strain offset chosen as $\Delta\varepsilon_{eq}^{p} = 0.1\%$.

Transmission Electron Microscopy method

After testing, two thin foils were taken, in a hot cell, from the specimen AT-IP. Small tiles were cut out of the thin tube, then mechanically polished and eventually double-jet electro-polished in a glove box using a Struers Tenupol with a solution of 90% ethanol and 10% perchloric acid at 5°C. Conventional Transmission Electron Microscopy was then conducted on a JEOL2100 operating at 200 kV. A double-tilt sample holder was used to observe the grains, with different diffraction vectors and different points of view with respect to the orientation of the grain.

Results of the mechanical tests

Evaluation of the elastic properties

It is often noticed that the elastic anisotropy of zirconium alloys rolled tubes is weak in the $\theta - z$ plane. It is thus convenient to consider that the behavior is isotropic, characterized by the Young's modulus (E) and the Poisson's ratio (ν). The mean value of the Young's modulus measured during the axial tensile tests is equal to 83 GPa. The mean value of the elastic slope measured during internal pressure tests is equal to 112 GPa. From the elastic slope during internal pressure tests, the Poisson's ratio is found to be of the order of 0.42, according to the formula given in (Onimus et al., 2018). These values are in correct agreement with values reported in the literature. For example, from their experiments on Zircaloy-4 containing 1000 ppm oxygen, Northwood and Rosinger (Northwood and Rosinger, 1980) found a Young's modulus of 77 GPa at 350°C. A value of 78 GPa at 350°C was also obtained by Delobelle et al. (Delobelle et al., 1996) on recrystallized Zircaloy-4. At 315°C, Schwenk et al. (Schwenk et al., 1978) obtained a Poisson's ratio of 0.41. This last parameter does not seem to evolve much with temperature. For their modeling, Delobelle et al. (Delobelle et al., 1996) used a Poisson's ratio of 0.4 at 350°C for recrystallized Zircaloy-4. In the following, a value of 0.4 is used for the Poisson's ratio, and values close to 80 GPa are used for the Young's modulus.

Analysis of the kinematic hardening and isotropic softening

In order to analyze the kinematic hardening, the second steps of each test have been compared to the first steps of each test. Indeed, as one can see on Figure 1b, if the material exhibits kinematic hardening, a prior axial tensile test should lead to a reduced yield stress during the subsequent internal pressure test. For this purpose, the stresses (hoop or axial) are plotted as a function of the translated equivalent plastic strain on Figure 4. The IP-AT test is shown as thick blue continuous lines and the test AT-IP as thin blue continuous lines.

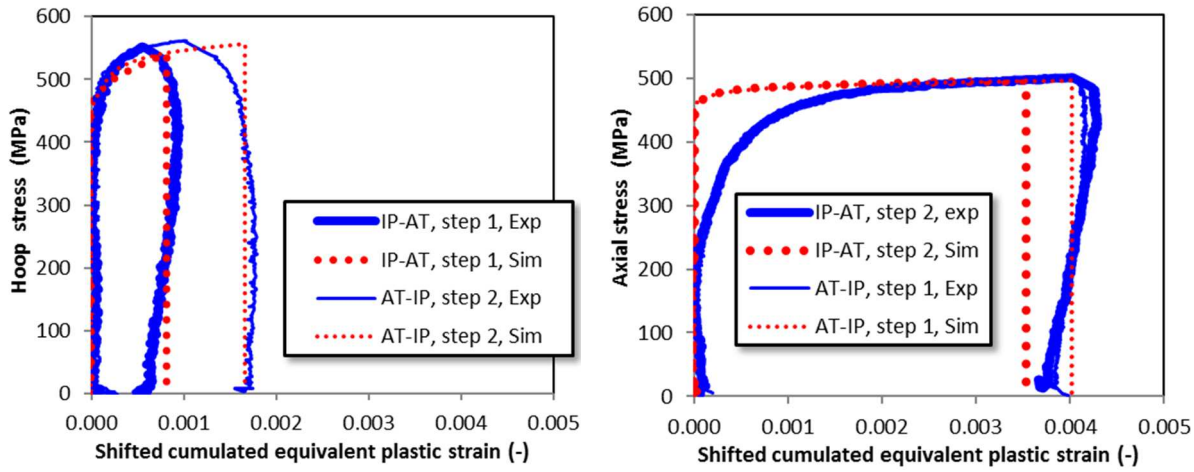

a) b)

Figure 4: Comparison between the first and second steps of a) internal pressure test, b) axial tensile test. The stress is shown as a function of the shifted cumulated plastic strain. The IP-AT test is shown as thick blue lines and the AT-IP test is shown as thin blue lines. The simulations are shown in red dotted lines.

It can be seen in Figure 4a that the second step of test AT-IP performed with internal pressure loading is very similar to the internal pressure test performed without a prior test (the first step of test IP-AT). Only the strain increment is different, but the evolution of the stress is the same. This suggests that the internal pressure test has not been noticeably affected by the prior axial tensile test. This is also true for the axial tensile tests (Figure 4b). Consequently, there is no clear evidence of the kinematic hardening during these tests.

As it was done in (Onimus et al., 2018) (Onimus et al., 2006), it is also interesting to analyze the unloading during the internal pressure tests. During the unloading, a phenomenon similar to the Bauschinger effect may be observed. If the kinematic stress component in the considered loading direction exceeds the isotropic stress ($X > R$), plastic deformation can occur at the end of the unloading (Feaugas, 1999). This phenomenon can be evidenced by a non-linearity on the stress-strain curve during the unloading and can be best observed when the stress is plotted as a function of the plastic strain (or cumulated equivalent plastic strain). Figure 5 shows the stress as a function of the cumulated equivalent plastic strain enlarged over a strain range of 0.5 % to show the unloading of step 11 of the test IP-AT and the unloading of step 12 of the test AT-IP, as examples. Indeed, for these late steps, the effect must be more evident than for previous steps. However, when looking carefully to the experimental results, no significant non-linearity of the unloading can be observed in Figure 5. This is also true for all other internal pressure steps. This result is in good agreement with what was already

observed in (Onimus et al., 2006). Although this method must be considered with care, this result suggests that the component of the kinematic stress tensor (X) remains lower than the isotropic stress (R) in this loading direction.

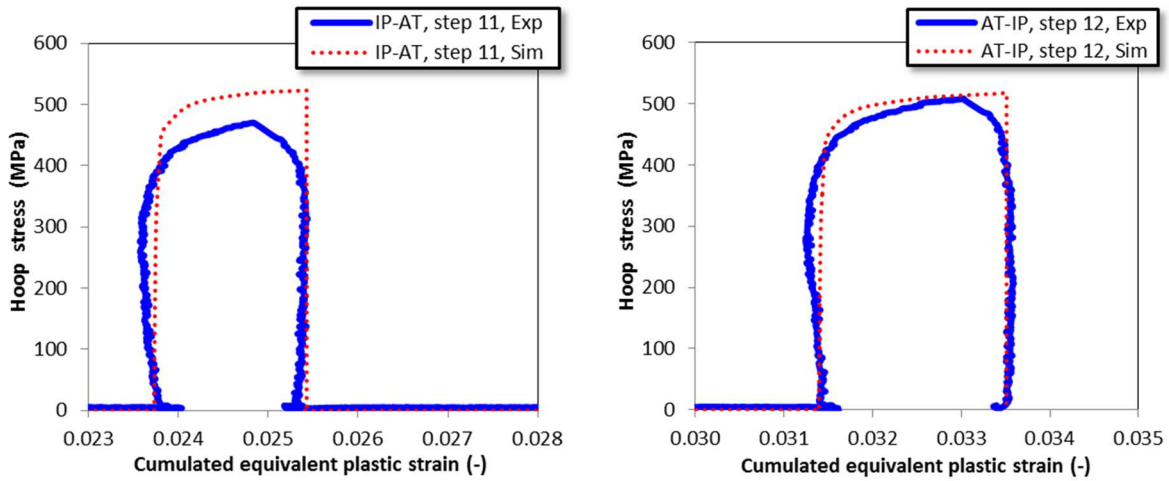

a) b)

Figure 5 : Hoop stress, during internal pressure steps, as a function of the cumulated equivalent plastic strain enlarged over a strain range of 0.5 %. a) Step 11 of the test IP-AT and b) step 12 of the test AT-IP. The result of the simulation using the polycrystalline model is also plotted.

In order to study the effect of the successive cycles, the axial and hoop stresses are represented as function of the equivalent cumulated plastic strain in Figure 6.

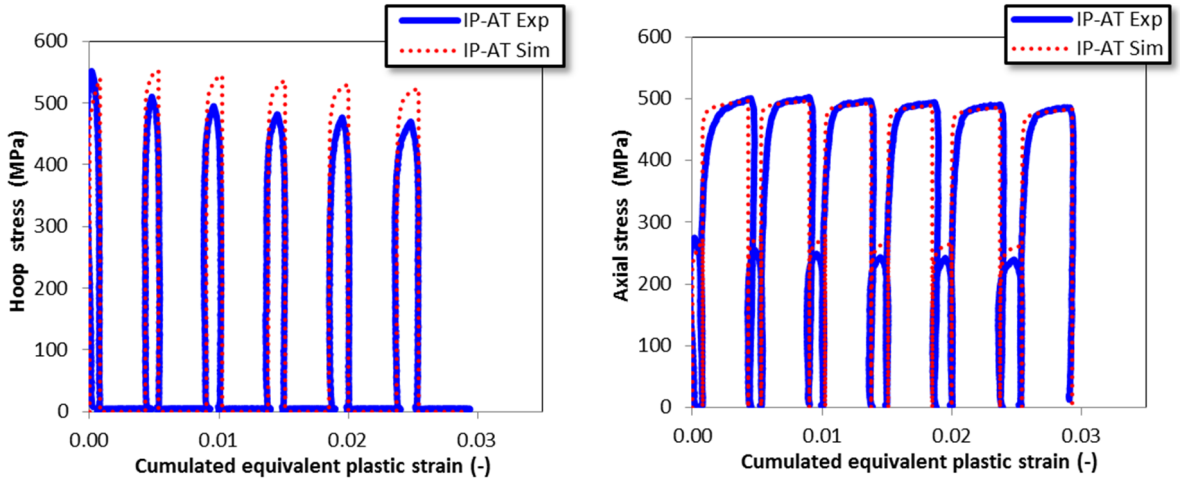

a) b)

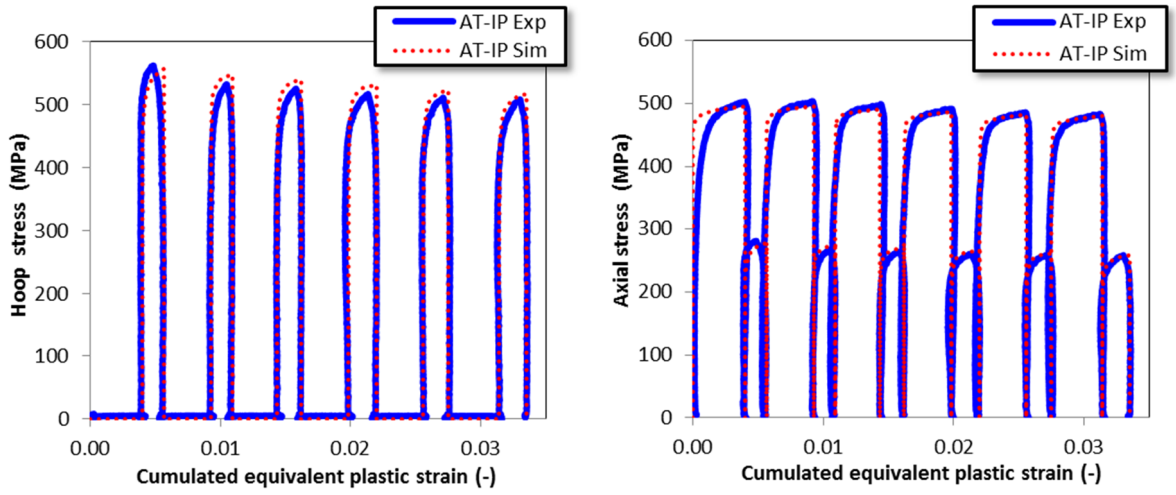

c) d)

Figure 6: Stress (hoop or axial) as a function of the cumulated equivalent plastic strain for the two tests. The experimental result is shown as a blue continuous line and the result of the simulation is shown as a red dotted line.

When analyzing the cyclic behavior during internal pressure tests, a striking phenomenon can be noticed. A significant decrease of the maximum stress is observed as the cumulated plastic strain increases (from 548 to 468 MPa for test IP-AT, and from 562 to 508 MPa for test AT-IP, which corresponds to a decrease of 80 and 54 MPa respectively). On the other hand, during axial tensile tests, the decrease of the maximum stress remains limited (from 500 to 485 MPa for test IP-AT and from 503 to 481 MPa for test AT-IP, which corresponds to a decrease of only 15 and 22 MPa respectively).

The flow stress for a plastic strain offset of $\Delta\varepsilon_{eq}^{p} = 0.1\%$, has been plotted as a function of the equivalent cumulated plastic strain. It can be seen that for the internal pressure tests, the hoop flow stress decreases as the cumulated equivalent plastic strain increases. More precisely, for a flow stress at 0.1% offset plastic strain, the decrease is equal to 80 MPa for test AT-IP test. Concerning the flow stresses measured in the axial direction during the axial tensile tests, the flow stress for an offset of 0.1%, increases of 20 MPa for test IP-AT and decreases of 6 MPa for test AT-IP. No trend can therefore be deduced from this last plot, the flow stress for these two offsets being nearly constant.

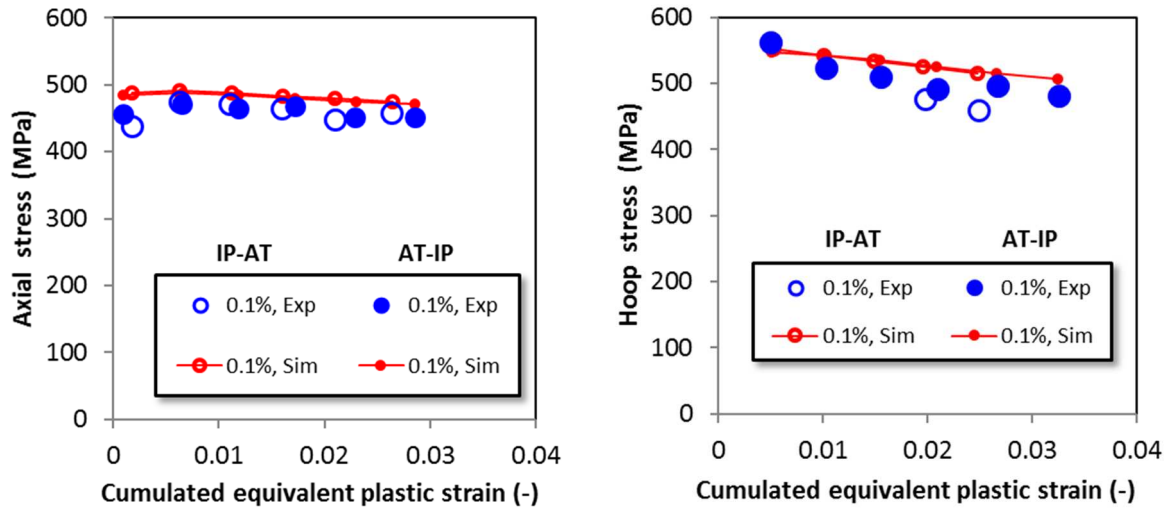

Figure 7: Evolution, as a function of the cumulated equivalent plastic strain, of the flow stress (axial or hoop) measured for an equivalent plastic strain offset of 0.1% for the tests conducted on neutron-irradiated Zr1%Nb. The simulated evolutions of the flow stress during the cyclic tests are also shown.

Results of the Transmission Electron Microscopy observations

TEM observations, done after the AT-IP mechanical test conducted on neutron-irradiated Zr1%Nb alloy, show numerous small <a>-loops in high density (figure 7a). Furthermore, when using a g=0002 diffraction vector few <c>-component loops are also observed, as long black segments, along with fine beta-niobium nano-precipitates induced by irradiation and native coarser beta-niobium precipitates (figure 7b). These observations are in good agreement with what is commonly observed in as-irradiated Zr1%Nb alloy (Onimus and Béchade, 2012) (Doriot et al., 2005) (Bossis et al., 2009) (Doriot et al., 2014) (Doriot et al., 2018).

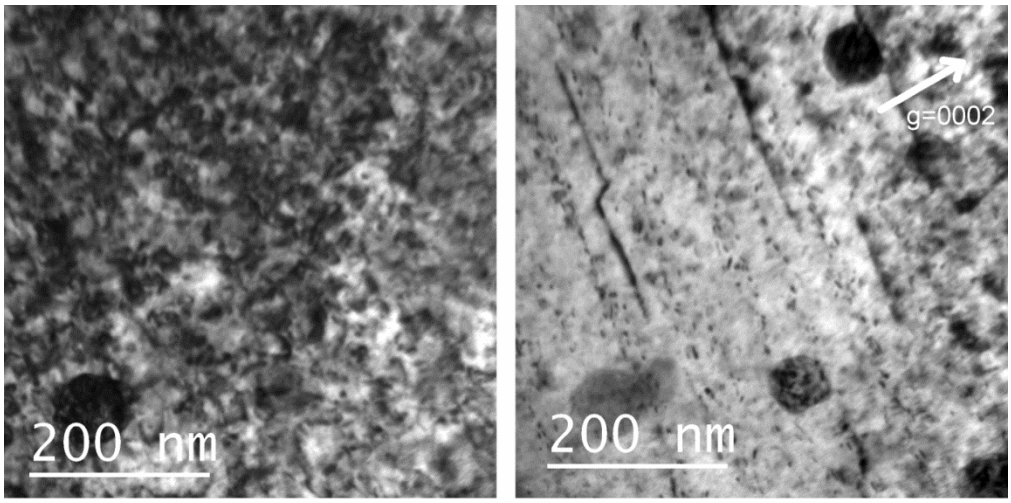

Figure 8: a) Numerous <a>-loops, b) <c>-component loops, beta-Nb nano-precipitates and native coarser beta-Nb precipitates observed with diffraction vector g=0002.

The most striking feature, which can be attributed to the mechanical test, was the observation of cleared bands also called dislocation channels. A careful analysis has been conducted to analyze the gliding planes corresponding to these channels. The method used was the same as the one described in (Onimus et al., 2004) (Onimus et al., 2005) (Onimus et al., 2012). From the orientation of the traces of the channels and from the knowledge of the tilt corresponding to the edge-on observation of the channel, the gliding plane is deduced. Nevertheless, it is often difficult to distinguish between prismatic and pyramidal channels since the traces are often close to each other, and furthermore the planes are observed edge-on for close orientations.

In the two thin foils studied, 38 grains have been analyzed and it was noticed that 28 out of these 38 grains contained dislocation channels. In 9 grains, basal channels were observed and in 19 grains prismatic or pyramidal channels were observed. Although it is difficult to unambiguously assess the habit plane of the channels in this last case, it seems that for 11 grains out of these 19 grains, channels were prismatic channels. For 3 grains, channels were pyramidal channels, and for 5 grains, it was not possible to distinguish between prismatic and pyramidal habit planes.

Images showing a wide basal channel are given in figure 8. It can be seen that the basal channel is predominantly parallel to the basal plane as shown by the g-vector, also parallel to the “walls” made of beta-Nb nano-precipitates and the “corduroy” contrast. The channel exhibits a bending probably due to the cross-slip of <a>-dislocations, from the basal plane to the prismatic or pyramidal plane. Observed at high magnification, this basal channel appears to be well cleared (figure 8b).

Images showing prismatic channels are given in figure 9. In that case, the channels appear straight and do not exhibit any cross-slip. Observed at high magnification (figure 9b), the prismatic channel seems to be full of entangled linear dislocations. The image observed at high magnification (figure 10b), for the grain containing pyramidal channels also exhibits entangled dislocations within the channel.

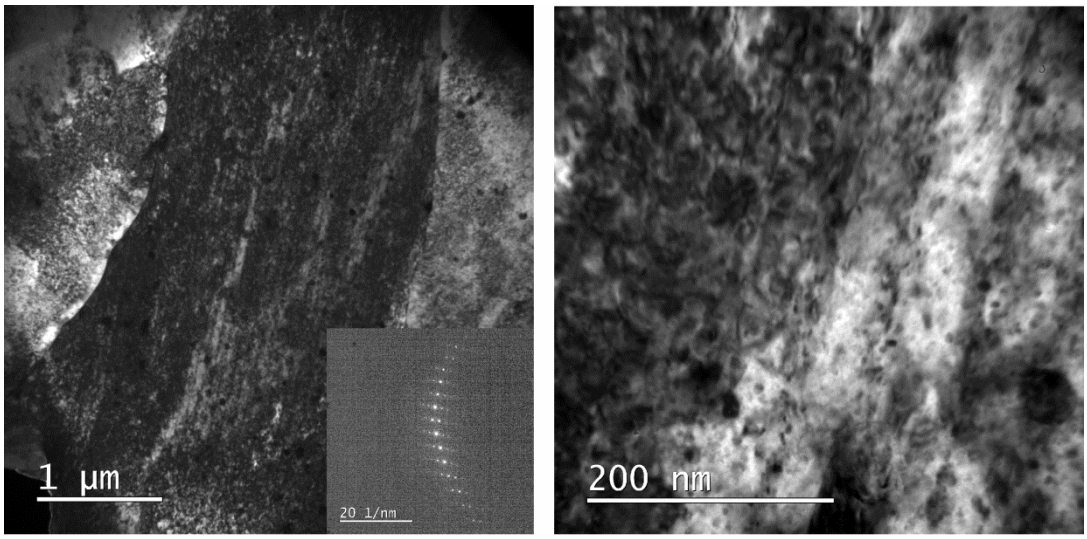

Figure 9: Dislocation channels in the basal plane observed at a) low magnification, b) high magnification, with an orientation such that the electron beam is close to the zone axis B~$\langle 11\bar{2}0\rangle$ using a diffraction vector g=$10\bar{1}0$.

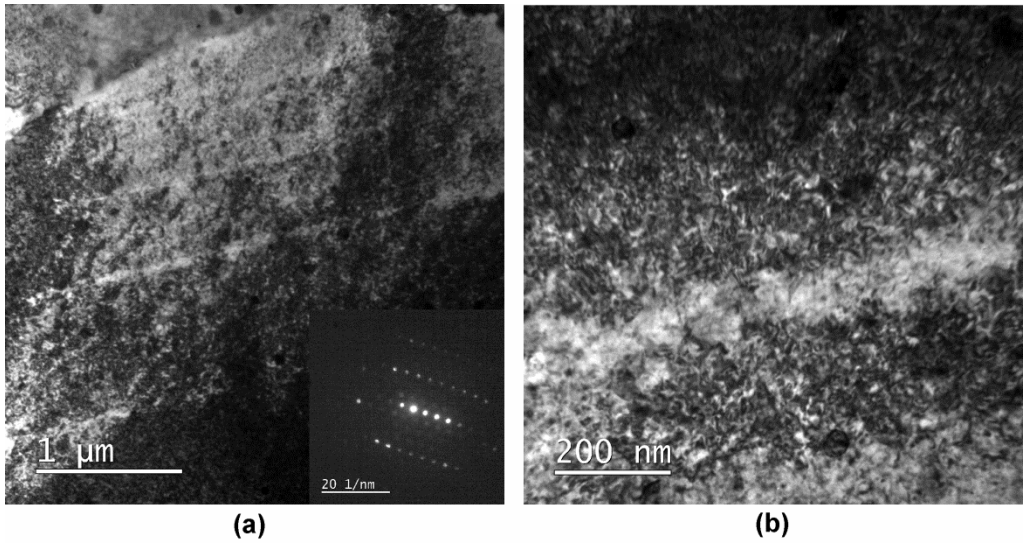

Figure 10: Dislocation channels in the prismatic plane observed at (a) low magnification, (b) high magnification with an orientation such that the electron beam is close to the zone axis B~$[0001]$ using a diffraction vector g=$10\bar{1}0$.

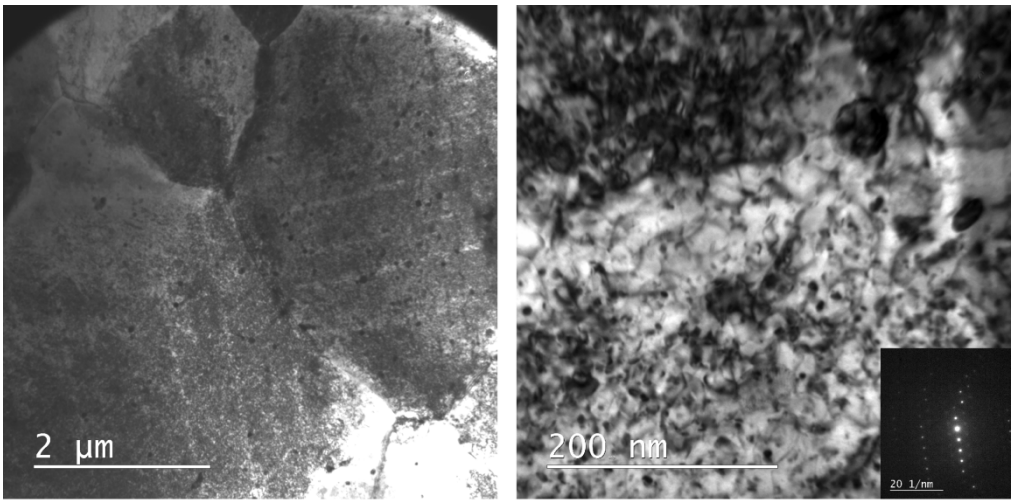

Figure 11: Dislocation channels in the pyramidal plane, observed at (a) low magnification, (b) at high magnification in the grain on the right of the picture shown in (a). The picture (b) is obtained with an electron beam close to the zone axis axis B~$\langle 11\bar{2}3\rangle$ using a diffraction vector g=$1\bar{1}01$.

Discussion on TEM observations

It is well known that neutron irradiation strongly affects the microstructure of zirconium alloys by creating a high density of small <a>-loops. These loops act as obstacles against dislocation glide and lead to strong irradiation-induced hardening. However, for a sufficient applied stress, these obstacles can be cleared by the gliding dislocations, creating zones free of defects, the dislocation channels, where further dislocations can glide easily. Previous TEM observations done after internal pressure tests conducted at 350°C on neutron-irradiated recrystallized zirconium alloys have been able to show channels in the basal plane (Onimus et al., 2004), but no channels were found in prismatic planes. This proved that basal slip is easier than prismatic slip after irradiation. This has been interpreted in terms of interactions between gliding dislocations and radiation induced loops. When a dislocation glides in the basal plane, the junction created with the loop is glissile, and the glide cylinder of the loop is parallel to the basal gliding plane. On the other hand, when the dislocation glides in the prismatic plane, the junction created is sessile, and the loop glide cylinder is not parallel to the gliding plane of the dislocation. This explains the stronger hardening of prismatic slip and the reduced ability to clear loops compared to basal slip. Furthermore, the three basal slip systems can contribute to clearing the basal channel, whereas only one prismatic slip system can contribute to create the prismatic channel.

This analysis has recently been confirmed and improved using dislocation dynamics simulations (Drouet et al., 2014). It has been shown that when a dislocation gliding in the prismatic plane encounters a <a> loop, in three cases out of six, a helical turn is formed, which is a strong pinning point

for the screw dislocation. On the other hand, if the dislocation glides in the basal plane, in five cases out of six, the loop can be easily dragged away by the dislocation.

Despite the difficult clearing of loops by prismatic glide, TEM observations done previously (Onimus et al., 2004) (Onimus et al., 2005) have revealed that when the basal plane is not well orientated for slip, which is the case for axial tensile tests, prismatic slip and <a>-pyramidal slip occur. In that case, prismatic and pyramidal channels are observed, but these channels did not seem as well cleared as basal channels, which is consistent with the analysis in terms of dislocation and loop interactions.

The TEM observations presented in this paper are in good agreement with these previous observations. Indeed, since both internal pressure tests and axial tensile tests have been conducted on the specimen analyzed, channels have been created in the basal, prismatic, and pyramidal planes.

Discussion of the mechanical test results in the light of deformation mechanisms

Discussion on the kinematic hardening

It is known that non-irradiated zirconium alloys exhibit a strong kinematic hardening because of a so-called "composite effect". Indeed, the plastic behavior of the individual h.c.p crystalline grains is anisotropic. The prismatic slip systems with <a> glide direction are easily activated, whereas the first order pyramidal planes with <c+a> glide direction are very difficult slip systems. The deformation of the grains along the <c>-axis is therefore very difficult. During mechanical tests, the well orientated grains for <a> glide deform plastically, but the poorly orientated grains for <a> glide remain elastic. A Bauschinger effect then arises (MacEwen et al., 1981) (Christodoulou, 1989). In the case of neutron-irradiated zirconium alloys, a significant Bauschinger effect is also reported after low cycle fatigue test (Wisner et al., 1994). It is mostly due to this composite effect. An additional phenomenon is also believed to increase the kinematic hardening. The dislocation channeling phenomenon leads to a localization of the plastic strain within the channels. The localization of the plastic strain is believed to induce strain incompatibilities at the tips of the channels leading to back stresses and thus an additional kinematic hardening.

During our tests conducted on neutron-irradiated samples, kinematic hardening was also suspected to occur. However, the influence of the prior loading did not induce any significant effect on the subsequent tests suggesting that the kinematic hardening is in fact very limited during these tests. This is confirmed by the shape of the unloading during the internal pressure steps (figure 3). Since no non-linearity was observed during the unloading, this proves that the kinematic stress component in this direction (X) remains lower than the isotropic stress (R).

The tests also showed a flow stress that decreases at each cycle for every plastic strain offset. This phenomenon can be interpreted as a progressive shrinkage of the yield surface as the cumulated plastic strain increases. In other words, this phenomenon is due to an “isotropic” strain softening. However, when analyzing each step independently, a typical strain hardening behavior is observed. This macroscopic strain hardening during monotonic tests can be explained by considering that the kinematic hardening balances the “isotropic” softening during monotonic tests, but as the cyclic test proceeds, the maximum flow stress decreases. This phenomenon can then be considered as an indirect evidence of kinematic hardening.

To conclude, our experiments suggest that there is a limited kinematic hardening during plastic deformation of recrystallized zirconium alloys after irradiation. This kinematic hardening remains small compared to the high flow stress of the material. This will be further discussed in the last section of this paper using the polycrystalline model.

Discussion on the cyclic strain softening

Our mechanical tests have shown that a cyclic strain softening occurs for irradiated zirconium alloy cladding tubes, in good agreement with the cyclic strain softening observed by Wisner et al. (Wisner et al., 1994) during tension-compression tests. This cyclic softening can be attributed to the clearing of loops by gliding dislocations during the dislocation channeling process. Because of the clearing of loops, a local strain softening occurs, inside the channels. During monotonic tests, this local strain softening is balanced by the kinematic hardening that arises because of the internal stresses present in the material at the polycrystalline scale. However, during cyclic tests, this local strain softening is evident.

The stronger cyclic strain softening observed during internal pressure tests, compared to the smaller softening observed during axial tensile tests, is nicely explained by the microscopic deformation mechanisms observed by TEM. Indeed, during internal pressure tests, basal slip is activated, whereas prismatic and <a>-pyramidal slip are predominant during axial tensile tests. Several experiments have shown that the dislocation channeling mechanism is easier in the basal plane than in the prismatic or pyramidal planes (Onimus et al., 2004) (Onimus et al., 2005). Furthermore, previous observations reported cleared basal channels and only partially cleared prismatic channels, in good agreement with the analysis of the interaction between dislocations and loops.

To summarize, during internal pressure steps, the basal slip is activated which induces a clearing of loops leading to a significant cyclic strain softening. During axial tensile steps, prismatic and <a>-pyramidal slips are mainly activated, inducing a less efficient clearing of loops and therefore a smaller degree of cyclic strain softening.

According to our TEM observations, an additional phenomenon seems to occur. Prismatic and pyramidal channels appear to contain many entangled linear dislocations. These dislocations may contribute to a strain hardening inside prismatic and pyramidal channels, which partially counteracts the strain softening occurring in these channels.

The fact that the second step of the test AT-IP, which corresponds to an internal pressure loading, is not affected by the prior axial tensile test can also be well understood in terms of deformation mechanisms. During the axial tensile test, prismatic and pyramidal channels are created, but this does not affect the subsequent creation of basal channels during the following internal pressure test. This is also true for the test conducted in the axial direction after an internal pressure test (step 2 of test IP-AT). The basal channels created during internal pressure tests do not affect the subsequent creation of prismatic channels. For this reason, the internal pressure steps and axial tensile steps are independent.

Polycrystalline Modeling

Principle of the polycrystalline model

The polycrystalline model used in this paper was first reported in (Onimus and Béchade, 2009) (Onimus et al., 2012). Many improvements have recently been made to the model. The principle of this type of model is to consider the material as a heterogeneous medium in the form of a polycrystalline aggregate. Then, from knowledge of the behavior of the individual grains and their orientations, the polycrystalline model is able to deduce the effective properties of the polycrystal (Kocks et al., 1998).

Crystallographic orientations used for the simulation

The crystallographic texture of the material (figure 1) is represented, in the modeling, by a set of 240 crystallographic orientations (figure 10). It has been verified, by introducing a more refined orientations set, that the results are only slightly modified (less than 3% increase in axial flow stress for axial tensile test).

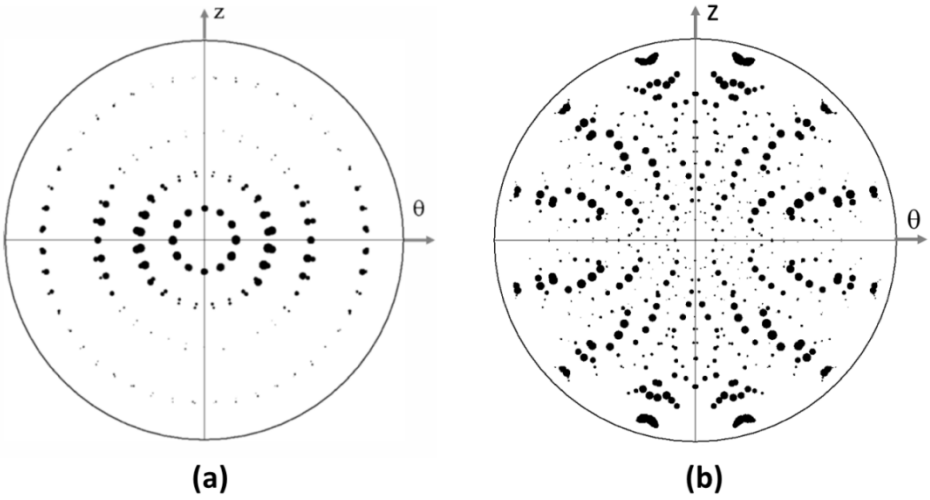

Figure 12: Discretized a) $\{0002\}$ and b) $\{11\bar{2}0\}$ pole figures representative of the texture of the material.

Homogenization procedure

The polycrystalline model used relies on a procedure first proposed by Cailletaud and Pilvin (Cailletaud, 1992) (Cailletaud and Pilvin, 1994) and then used by many researchers (Feaugas et al., 1997) (Barbe et al., 2001) (Hoc, 2001) (Diard et al., 2005) (Rousselier and Leclercq, 2006) (Vincent, 2008) (Evrard et al., 2008) (Priser et al., 2010) (Gérard et al., 2013). This procedure is based on a postulated explicit concentration rule (equations 3, 4 and 5) that relates the local stress $\left(\underline{\underline{\sigma_g}}\right)$ in the considered crystallographic phase (g) (all the grains with the same crystallographic orientation) to the macroscopic applied stress $\left(\underline{\underline{\Sigma}}\right)$.

$$\underline{\underline{\sigma_g}} = \underline{\underline{\Sigma}} + 2\mu(1-\beta)\left(\underline{\underline{B}} - \underline{\underline{\beta_g}}\right) \qquad (3)$$

with

$$\underline{\underline{B}} = \sum_{g\in G} f_g \underline{\underline{\beta_g}} \qquad (4)$$

and

$$\dot{\underline{\underline{\beta}}}_g = \dot{\underline{\underline{\varepsilon}}}_g^p - D\left(\underline{\underline{\beta_g}} - \delta\underline{\underline{\varepsilon}}_g^p\right)\left\|\dot{\underline{\underline{\varepsilon}}}_g^p\right\| \qquad (5)$$

In equation 3, μ is the shear modulus and β is given by equation 6, where ν is the Poisson ratio.

$$\beta = \frac{2(4-5\nu)}{15(1-\nu)} \qquad (6)$$

In equation 4, f_g refers to the volume fraction of each considered crystallographic phase (g).

In equation 5, $\dot{\underline{\underline{\varepsilon}}}_g^p$ refers to the local plastic strain rate and $\underline{\underline{\varepsilon}}_g^p$ to the current plastic strain. The tensor $\underline{\underline{\beta_g}}$ in equation 3 is an internal variable that evolves non-linearly with the local plastic strain ($\underline{\underline{\varepsilon}}_g^p$) of the crystallographic phase, according to Eq. (5). This mathematical formulation is well adapted to simulate

cyclic tests. This model is not itself self-consistent from the homogenization theory point of view. It has therefore been proposed to adjust the two parameters, D and δ, which govern the evolution of the internal variable $\underline{\underline{\beta_g}}$, on the local response of the model developed by Berveiller and Zaoui (Berveiller and Zaoui, 1978) which is self-consistent, thus ensuring that the model is close to a self-consistent model. More details on this procedure can be found in (Onimus and Béchade, 2009).

Crystal plasticity

At the grain scale, the mechanical behavior is governed by the glide of dislocations on various slip systems. Four types of slip systems are taken into account in the model:

- the three prismatic slip systems with <a> Burgers vector (P),
- the three basal slip systems with <a> Burgers vector (B),
- the six first order pyramidal slip systems with <a> Burgers vector (Πa),
- the twelve first order pyramidal slip systems with <c+a> Burgers vector (Πc).

The resolved shear stress on each slip system (τ_s) is computed, according to equation 7.

$$\tau_s = \frac{1}{2}\underline{\underline{\sigma_g}} : \left(\underline{n_s}\otimes\underline{m_s} + \underline{m_s}\otimes\underline{n_s}\right) \qquad (7)$$

In equation 7, $\underline{n_s}$ is the normal of the considered slip system and $\underline{m_s}$ is the glide direction of the considered slip system.

The plastic strain rate tensor for each crystallographic phase (g) undergoing shear strain on the various slip planes is expressed according to equation 8, where $\dot{\gamma}_s$ is the shear strain rate.

$$\underline{\underline{\dot{\varepsilon}_g^p}} = \frac{1}{2}\sum_{s\in S}\dot{\gamma}_s\left(\underline{n_s}\otimes\underline{m_s} + \underline{m_s}\otimes\underline{n_s}\right) \qquad (8)$$

Constitutive equations accounting for the effect of neutron irradiation

The shear strain rate on each slip system is governed by the flow law (equations 9 and 10).

$$\dot{\gamma}_s = \dot{v}_s \mathrm{sign}(|\tau_s - x_s| - \tau_s^c) \qquad (9)$$

$$\dot{v}_s = Max\left[0\ ;\ \left(\frac{|\tau_s - x_s| - \tau_s^c}{K}\right)^n\right] \qquad (10)$$

The function $\mathrm{sign}(x)$ can be defined as $\mathrm{sign}(x) = x/|x|$ and gives the sign of x. The parameters, n and K, chosen for this flow law (K = 5 MPa.s$^{1/n}$ and n = 10) are such that the model exhibits a very low strain rate sensitivity. In equation 9 and 10, τ_s is the resolved shear stress and τ_s^c the critical resolved shear stress. The local internal variable x_s that appears in equation 9 and 10 is a scalar algebraic quantity that induces a non-linear kinematic hardening at the grain scale as proposed by Méric et al. (Méric et al., 1994). Its evolution is given by equation 11.

$$\dot{x}_s = C_s\dot{\gamma}_s - D_s x_s \dot{v}_s \qquad (11)$$

With $x_s(0) = 0$ (12)

The effect of neutron irradiation on the behavior of the material is taken into account by the choice of the critical resolved shear stresses τ_s^c and their evolution. The effect of irradiation is mainly to create numerous small <a>-loops that act as obstacles against dislocation glide, in a similar way as "forest" dislocations. This hardening, at the slip system scale, can be simply accounted for by expressing (equation 13) the critical resolved shear stress as the sum of a constant critical resolved shear stress (τ_s^{c0}), that can be regarded as the non-irradiated critical resolved shear stress, and a term proportional to the square root of the linear dislocation loop density (ρ_s^l in m^{-2}), where ρ_s^l is simply expressed as equation 14.

$\tau_s^c = \tau_s^{c0} + \alpha_s^l \mu b_s \sqrt{\rho_s^l}$ (13)

$\rho_s^l = Nd$ (14)

In equation 14, N is the loop number density (in m^{-3}) and d is the mean loop diameter (in m). The quantity $1/\sqrt{\rho_s^l}$ corresponds to the mean distance between loops in the glide plane of a dislocation. The Burgers vector length is equal to $b_s = a$ for all slip systems with <a> Burgers vector. For pyramidal slip with <c+a> Burgers vector, the Burgers vector length is equal to $b_s = 1.88a$ (with $c/a = 1.593$).

The parameter α_s^l accounts for difference in the effective strength of the various interactions between the dislocation and the loop. In the case of basal slip, the effective strength of the interaction ($\alpha_s^l = \alpha_B^l$) is small since basal slip is more easily activated after irradiation. On the other hand, the effective strength between a loop and a dislocation gliding in the prismatic or pyramidal plane must be higher than the effective strength of basal slip ($\alpha_P^l > \alpha_B^l$, $\alpha_{\Pi a}^l > \alpha_B^l$).

Due to dislocation glide, a clearing of loops occurs within the dislocation channels. As shown in (Onimus et al., 2012) (Onimus et al., 2004) (Onimus et al., 2005) the clearing of loops is easy in the basal plane. Following the approach proposed in (Onimus and Béchade, 2009) (Onimus et al., 2005) the equation 15 describing the evolution of loops within the basal channels has been adopted.

$\frac{d\rho_s^l}{dt} = -k_B \rho_s^l [\sum_{s \in B} \dot{v}_s]$ (15)

Since all three basal slip systems have the same glide plane in the h.c.p lattice, the glide on one slip system contributes to the clearing of loops for the other slip systems. This is why the sum of the shearing rates on all three basal systems ($s \in B$) is taken into account in equation 15.

On the other hand, the decrease of the loop density in one prismatic channel does not affect the loop density in another prismatic slip system, or in the basal or pyramidal channels, the loop densities in these slip systems then evolve separately, in an uncoupled way, according to equation 16. This explains

why although physically, there is only one loop density per grain, it is necessary to distinguish the loop densities of the various slip systems.

$\frac{d\rho_s^l}{dt} = -k_s \rho_s^l \dot{v}_s$ for $s \in P \cup \Pi a$ (16)

Because the prismatic and pyramidal channels are less cleared than basal channels, the coefficient characteristic of the clearing capability must be lower for prismatic and pyramidal slip than for basal slip ($k_P < k_B$ and $k_{\Pi a} < k_B$).

It should also be mentioned that only few <c+a> dislocations have been observed, as reported in (Onimus et al., 2012). Pyramidal channels have not been associated with these dislocations. The clearing of loops by pyramidal <c+a> slip has not been observed and is thus not taken into account in the model. This slip system is only hardened by irradiation and its loop density does not evolve (equation 17).

$\frac{d\rho_s^l}{dt} = 0$ for $s \in \Pi c$ (17)

The initial loop density is the same for every slip systems, and is equal to $\rho_s^l(0) = N_0 d$ = 5×10^{14} m^{-2} with N_0=5×10^{22} m^{-3} and d =10 nm, in good agreement with TEM observations (Carpenter and Northwood, 1975).

Because of the significant clearing of loops in the basal channels, and the associated strong localization of the plastic strain inside these channels, it has been proposed (Onimus and Béchade, 2009) to introduce a kinematic hardening at the slip system scale for basal slip (equations 10, 11 and 12). Indeed, the localization of the plastic strain is believed to induce significant back stresses because of strain incompatibilities arising at the tip of the channels on the grain boundary. Concerning prismatic and pyramidal slip systems, because the clearing of loops appears to be limited, the associated strain localization may be also limited. Thus no intragranular kinematic hardening is taken into account for these slip systems ($x_s = 0$ for $s \in P \cup \Pi a \cup \Pi c$).

This model has 15 coefficients that must be adjusted to fit the experimental behavior of the material: the four initial critical resolved shear stresses ($\tau_P^0, \tau_{\pi a}^0, \tau_B^0, \tau_{\pi c}^0$), the four effective strengths of the dislocation loop interaction ($\alpha_P^l, \alpha_{\pi a}^l, \alpha_B^l, \alpha_{\pi c}^l$), three coefficients for the clearing of loops (k_P , $k_{\pi a}, k_B$), two coefficients for the basal intragranular kinematic hardening (C_B, D_B). The two parameters, D and δ, are also adjusted simultaneously on the response obtained, using the isotropic texture, with the Berveiller and Zaoui model (Berveiller and Zaoui, 1978) as described in (Onimus and Béchade, 2009).

Simulation procedure for the strain path change tests and fitting of the parameters

The mechanical tests have been simulated using the SiDoLo software, which was developed by Pilvin (Andrade-Campos et al., 2007) (Pilvin, 2010). The quasi-biaxial approach has been adopted for the simulation of the tests as described in (Onimus et al., 2018).

The tests are computed with constant axial strain rate for axial tensile tests or with constant hoop strain rate for internal pressure tests, in agreement with the experiments. For internal pressure tests, the axial stress must be equal to half of the hoop stress. However, the hoop stress is initially unknown since it is the outcome of the simulation. Therefore, an iterative procedure has been adopted where the tests are simulated several times before converging to the required biaxiality ratio. Furthermore, a specific procedure ensures that each step starts and ends with zero stress, as for the experiment, and that each step smoothly follows its predecessor.

Because the hoop extensometers did not correctly measure the reduction in diameter during the axial tensile tests, the evaluation of the agreement between simulation and experiment has been done by comparing the flow stress values for each step as a function of the cumulated equivalent plastic strain (Figure 6). The cumulated equivalent plastic strain is computed for the simulation in exactly the same way as for the experiment. Only the test AT-IP has been used for the refinement procedure.

Starting from previous parameters obtained with more simple constitutive equations (Onimus and Béchade, 2009), the critical resolved shear stresses, the strain softening parameters and the kinematic hardening parameters have been adjusted. Initially, only the first monotonic steps of each test are computed, compared with the experiment and used for the refinement. Then some parameters are slightly modified to obtain the correct flow stress, as a function of the cumulated plastic strain, all along the full AT-IP cyclic test. At the end of this refinement procedure, one set of parameters is obtained (Table 4). It should be pointed out that other coefficients sets may also give correct agreement between simulations and experiments.

Table 3: Parameters and values obtained after refinement for the neutron-irradiated material.

Parameter (unit)	Value for neutron-irradiated material
$\boldsymbol{E}$ (MPa)*	80000
$\boldsymbol{\nu}$ (-)*	0.4
$\boldsymbol{n}$ (-)*	10
$\boldsymbol{K.s^{1/n}}$ (MPa)*	5
$\boldsymbol{D}$ **(-)**	280
$\boldsymbol{\delta}$ **(-)**	0.53
$\boldsymbol{\tau_P^0}$ **(MPa)**	61
$\boldsymbol{\tau_{\pi a}^0}$ (MPa)	76
$\boldsymbol{\tau_B^0}$ (MPa)	105
$\boldsymbol{\tau_{\pi c}^0}$ (MPa)	140
$\boldsymbol{\alpha_P^l}$ (-)	0.80

$\alpha_{\pi a}^{I}$ (-)	0.80
α_{B}^{I} (-)	0.50
$\alpha_{\pi c}^{I}$ (-)	0.41
k_{P} (-)	14.0
$k_{\pi a}$ (-)	4.7
k_{B} (-)	120.0
C_{B} (MPa)	10 000
D_{B} (-)	200
$\rho_{s}^{I}(\mathbf{0})$ (m^{-2})*	5×10^{14}

Results of the simulations and discussion

It can be seen on Figure 6 that this polycrystalline model captures very well the main macroscopic phenomena occurring during the strain path change test AT-IP conducted on neutron-irradiated Zr1%Nb alloy. The evolution of the flow stress as a function of cumulated equivalent plastic strain is well reproduced.

The maximum flow stresses for both internal pressure steps and axial tensile steps are well reproduced by the model and especially the significant cyclic strain softening during internal pressure steps and the lower softening during the axial tensile steps. However, although the maximum flow stress is correctly reproduced for axial tensile test, the yield is not correctly reproduced. The model predicts a very sharp yield whereas it is more progressive in the experiment. Concerning internal pressure steps, both the yield and the maximum stresses are correctly reproduced.

The behavior recorded during the test IP-AT differs slightly from the behavior observed during the test AT-IP. Thus, the model adjusted on the test AT-IP cannot reproduce perfectly the behavior of the IP-AT test. However, the qualitative trend is correctly simulated.

It must also be noticed that

Assuming that a single slip system is activated on the basal plane, and on the other planes, the evolution of the critical resolved shear stresses (τ_s^c) as a function of the shear strain (γ_s) on the considered slip system can be plotted (Figure 13). Since for basal slip, a kinematic hardening has been added at the slip system scale, it is interesting to plot the evolution of this kinematic hardening (x_s), also added to the critical resolved shear stress ($x_s + \tau_s^c$), as a function of the shear strain.

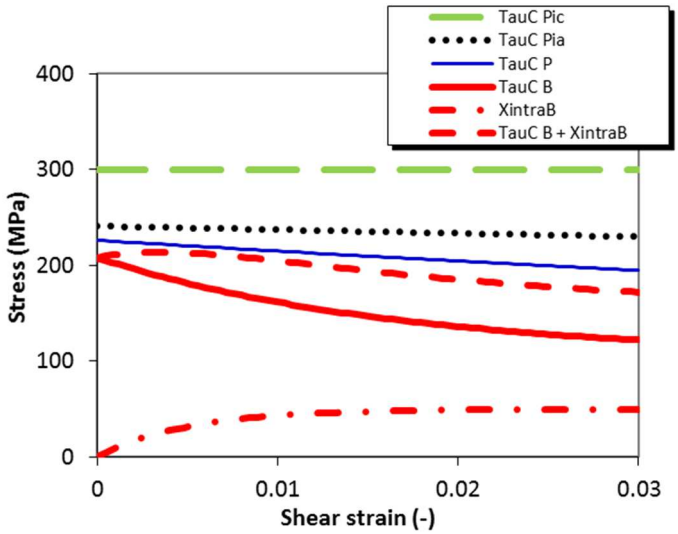

Figure 13: Evolution of the critical resolved shear stresses (τ_s^c) as a function of the shear strain (γ_s) assuming single slip activation for the four types of slip systems. For basal slip is also shown: the intragranular kinematic stress (x_s) added to the critical resolved shear stress ($x_s + \tau_s^c$).

It can be noticed on Figure 13 that the intragranular kinematic hardening on the basal plane balances the decrease of the critical resolved shear stress up to 0.4% shear strain. It can also be noticed that the critical resolved shear stress on the prismatic plane is in fact rather close to the sum of the critical resolved shear stress and kinematic stress on the basal plane.

Before going further, it is very interesting to use the model to compute the overall slip system activities, as defined in (Onimus and Béchade, 2009), during internal pressure tests and axial tensile tests. The slip system activity of the system of type T (A_T), T being successively equal to $P, \pi a, B, \pi c$, is expressed by equation 18 and 19.

$$a_T = \sum_{g \in G} f_g \sum_{r \in T} \dot{v}_r \qquad (18)$$

Computing successively the values for a_T for all four types of slip systems, allows the computation of the sum of these values ($\sum_{T \in S} a_T$) over all the slip systems ($S = P \cup \pi a \cup B \cup \pi c$). Then, the percentage of slip system activity over the whole polycrystal (A_T) can be computed for each type of slip system:

$$A_T = \frac{a_T}{\sum_{i \in S} a_i} \qquad (19)$$

The activities (A_T) of the various slip systems (before the unloading) during the two first steps and the two last steps of the test AT-IP are reported in Table 4.

Table 4: Slip system activities computed during four steps of the AT-IP test.

Step	Loading direction	Prismatic	Pyramidal-<a>	Basal	Pyramidal-<c+a>
1	AT	69%	23%	7%	0%
2	IP	1%	2%	75%	22%
11	AT	66%	18%	13%	4%
12	IP	1%	2%	66%	31%

It can be seen that during internal pressure tests, the active slip is predominantly in the basal plane, in good agreement with what was observed by TEM during previous experiments (Onimus et al., 2012) (Onimus et al., 2004) (Onimus et al., 2005). As expected, during axial tensile tests, basal slip is rare, and slip occurs primarily in the prismatic and <a>-pyramidal planes, which is also in good agreement with what was previously observed (Onimus et al., 2004) (Onimus et al., 2005). With this in mind, one can look carefully at the detailed response of the model in terms of i) cyclic strain softening and ii) kinematic hardening.

i) The rapid cyclic strain softening of AT-IP test for internal pressure is well reproduced thanks to the introduction of the rapid clearing of loops when basal slip is activated. This slip system is indeed mainly activated for this loading direction. During monotonic tests, the strain softening is partly balanced by the intragranular kinematic hardening and by the intergranular kinematic hardening resulting from the interaction between grains. Thus, we succeed in having an overall strain hardening behavior during the monotonic tests and at the same time a cyclic strain softening during the strain path change tests.
The low cyclic strain softening for axial tensile test is also well reproduced thanks to the introduction of the low clearing of loops when the prismatic and <a>-pyramidal slip systems are activated, which is the case for axial tensile tests.
Furthermore, the fact that the two loading directions are independent is well reproduced by the model. The significant strain softening occurring during internal pressure tests, which is due to the clearing of loops in the basal channels, does not affect the subsequent behavior during axial tensile test where primarily prismatic and <a>-pyramidal slip are active.

ii) Concerning the kinematic hardening, it must be noted that the model reproduces the linearity during the unloading for internal pressure tests, even for the last steps of the AT-IP and IP-AT tests (Figure 5). This phenomenon was explained by the fact that the kinematic hardening (the translation of the yield surface) is too small compared to the isotropic stress (the size of the yield surface). This has been investigated further thanks to the polycrystalline model.

The evolution of the yield surface during the strain path change tests has been computed. An offset of 0.1% for the equivalent plastic strain is chosen to plot the yield surface. The equivalent plastic strain is

calculated, for each biaxiality ratio, according to equation 20. It has been checked that the difference with the computation used previously is small.

$$\varepsilon_{eq}^{p} = \int_0^t \dot{\varepsilon}_{eq}^{p}\, dt = \int_0^t \sqrt{\frac{2}{3}\dot{\boldsymbol{\varepsilon}}^{p} : \dot{\boldsymbol{\varepsilon}}^{p}}\, dt \quad (20)$$

First, the initial yield surface is computed. Then, the yield surface after 11 steps of the AT-IP test is computed. These yield surfaces are reported on the Figure 14. On this plot, two experimental values of the flow stresses at 0.1% equivalent plastic strain during internal pressure tests are also reported: the step 2 and the step 12 of the AT-IP test (cf. Figure 7).

A reduction of the size of the yield surface is observed, because of the cyclic strain softening. However, interestingly, this reduction is anisotropic. The reduction is small in the axial direction and more significant in the hoop or internal pressure directions. This is because the clearing of loops is easier for basal slip and more difficult for prismatic and <a>-pyramidal slip.

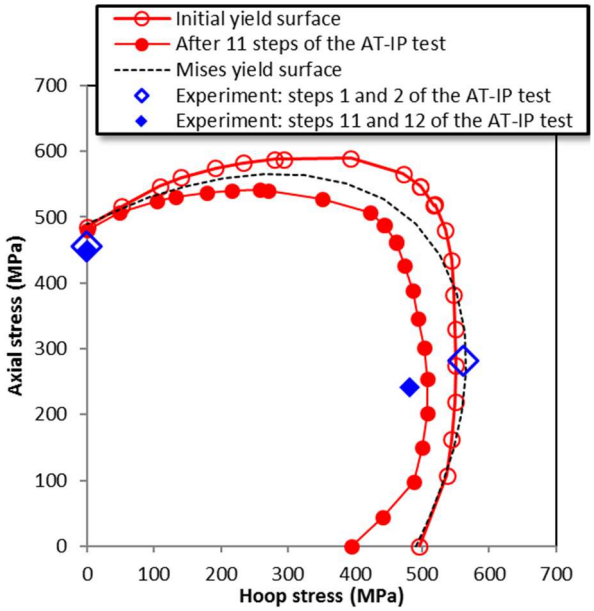

Figure 14: Simulation of the evolution of the yield surface during the strain path change tests. Comparison between the initial yield surface and the yield surface after the full AT-IP test. The offset chosen to compute the yield surface is 0.1%. Experimental values are also shown on this plot.

Kinematic hardening was not observed during our experiments. Nevertheless, Wisner et al. (Wisner et al., 1994) have shown a Bauschinger effect using tension-compression tests in the transverse direction of a neutron-irradiated recrystallized zirconium alloy. It is therefore interesting to see whether our polycrystalline model is consistent with these previous experimental results. Using the polycrystalline model developed, the tension-compression tests were simulated. The stress in the transverse direction is plotted as a function of the plastic strain (Figure 15) and compared to the stabilized hysteresis loop given in (Wisner et al., 1994). There is a good agreement between the model and the reported

experimental observations. Furthermore, the maximum stress is computed all along the cyclic test. A decrease of the maximum stress is reproduced in correct agreement with the initial maximum stress and the steady state maximum stress given in (Wisner et al., 1994). It is possible to go even further by analyzing the simulated tension-compression loops in terms of kinematic hardening (X), or back stress, and isotropic stress (R), or friction stress, following the method described in (Li et al., 2003) (Feaugas, 1999) (Dickson et al., 19984). An offset of 0.1% is also considered for the calculation of the yield stress during compression. It can be seen that the isotropic stress (R) decreases all along the test and the kinematic stress (X) increases at the beginning then reaching a plateau. It can also be noticed that the kinematic stress remains significantly lower (110 MPa) than the isotropic stress (220 MPa), as discussed previously.

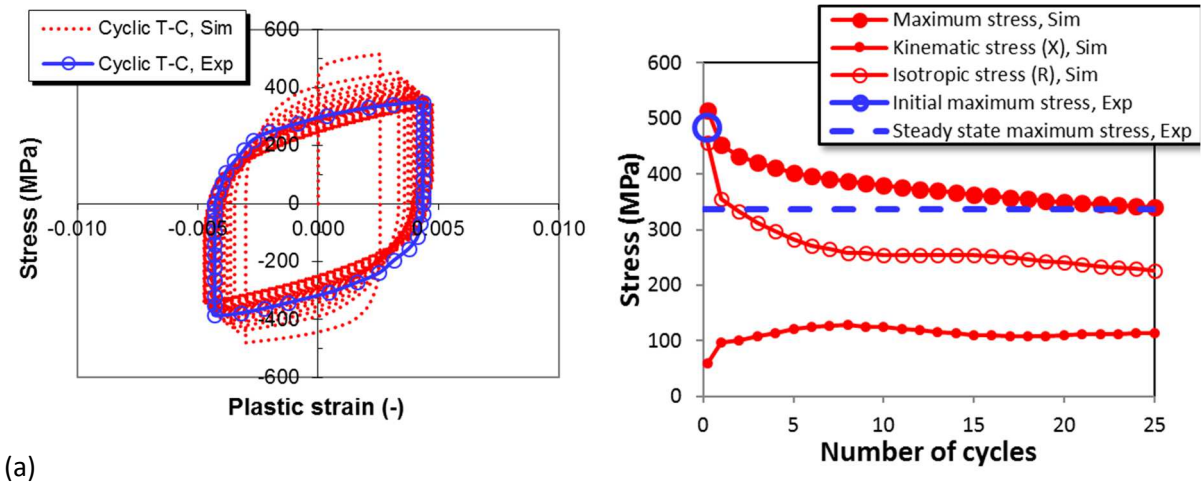

(a)

(b)

Figure 15: Simulation of cyclic tension-compression (T-C) test and comparison with experiments. a) Stress as a function of plastic strain and comparison with the stabilized hysteresis loop given in (Wisner et al., 1994). b) Simulated maximum stress as a function of the number of cycles and comparison with the initial maximum stress and the steady state maximum stress given in (Wisner et al., 1994). The simulated kinematic and isotropic stresses are also reported in this plot. The detection offset chosen to compute the kinematic stress (*X*) and the isotropic stress (*R*) is equal to 0.1%.

Conclusion

Strain path change tests have been conducted at 350°C on thin tube samples made of neutron-irradiated Zr1%Nb alloy. These tests consist of alternate internal pressure tests and axial tensile tests. During the internal pressure test steps, the flow stress exhibits a cyclic strain softening. This is attributed to efficient clearing of loops by dislocations gliding in the basal plane, a slip system which is easily activated during internal pressure tests on neutron-irradiated recrystallized zirconium alloys at 350°C. However, only a small degree of cyclic strain softening has been observed during axial tensile tests. This is attributed to the limited clearing of loops by dislocations gliding in the prismatic and

pyramidal planes, that are mainly activated during axial tensile tests at 350°C, after neutron irradiation. TEM observations conducted after the mechanical tests have confirmed this analysis.

A polycrystalline model has been used to simulate these tests. By introducing the clearing of loops into the model, it is able to reproduce many features of the complex behavior observed during the experiments. The prediction of the slip system activation is also in good agreement with TEM observations. Furthermore, the model is able to reproduce correctly some data available in the literature such as cyclic tension-compression test. This model also provides an interesting insight into the role of kinematic hardening on the mechanical behavior of neutron-irradiated recrystallized zirconium alloys.

Further improvements on this topic could be done, on the experimental side, by using High Resolution Digital Image Correlation on irradiated samples, as it has recently been done by Thomas et al. (Thomas et al., 2019) on proton irradiated zirconium alloys and, on the numerical side, by using advanced numerical tools such as the one recently developed by Gélébar et al. (Gélébart and Mondon-Cancel, 2013; Marano, et al., 2019) using Fast-Fourier Transform algorithms.

Acknowledgments: This work has been funded by the project GAINE from the French nuclear tripartite institute CEA EDF Framatome.

Appendix:

The stress state in the wall of a tube is triaxial ($\sigma_{rr},\ \sigma_{\theta\theta},\ \sigma_{zz}$). However, it can easily be shown that the radial component of the stress tensor (σ_{rr}) is small compared to the two other components. This radial component is often neglected leading to the well-known thin tube formula. A better approximation of the stress tensor can be obtained by using the approach described in (Onimus et al., 2018). In this approach, it is proposed to compute a so-called "quasi-biaxial" (with superscript "qb") hoop and axial stresses ($\sigma_{\theta\theta}^{qb},\ \sigma_{zz}^{qb}$) in the same way as in the thin-wall approximation, but without neglecting the radial stress, thus keeping the advantage of a simple analysis of the mechanical test.

$$\sigma_{\theta\theta}^{qb} = \sigma_{\theta\theta} - \sigma_{rr} = \frac{PD_m}{2e}$$

$$\sigma_{zz}^{qb} = \sigma_{zz} - \sigma_{rr} = \frac{PD_m}{4e} + \frac{F}{e\pi D_m}$$

In these formulas, P is the pressure, F is the axial force, D_m is the tube mean diameter ($D_m = 9.5$ mm) and e is the thickness ($e = 0.57$ mm).

The values computed above are the "engineer" stress values (with subscript "eng"). To compute the true stress values (with subscript "true"), it is necessary to take into account the evolution of the gauge length and the evolution of the thickness and mean diameter of the specimen throughout the test.

$$\left(\sigma_{\theta\theta}^{qb}\right)_{true} = (\sigma_{\theta\theta})_{true} - (\sigma_{rr})_{true} = \left(1 + (\varepsilon_{\theta\theta})_{eng}\right)$$

$$\left(\sigma_{zz}^{qb}\right)_{true} = (\sigma_{zz})_{true} - (\sigma_{rr})_{true} = \left(\sigma_{zz}^{qb}\right)_{eng}\left(1 + (\varepsilon_{zz})_{eng}\right)$$

Concerning the strain values, the engineering axial strain is computed according to the following formula.

$$\left(\varepsilon_{zz}\right)_{eng} = \frac{\Delta L(t)}{L(0)}$$

The true axial strain is computed according to the following formula.

$$\left(\varepsilon_{zz}\right)_{true} \approx ln\left(1 + \left(\varepsilon_{zz}\right)_{eng}\right)$$

A fair approximation of the mean hoop strain in the wall of the tube is obtained by using the following formula.

$$\left(\varepsilon_{\theta\theta}\right)_{eng} \approx \frac{\Delta D_{ext}(t)}{D_{ext}(0) - e(0)}$$

The true mean hoop strain is then computed as follows:

$$\left(\varepsilon_{\theta\theta}\right)_{true} \approx ln\left(1 + \left(\varepsilon_{\theta\theta}\right)_{eng}\right)$$

In this article, all the experimental values given are true stresses and true strains considering that the stress state is quasi-biaxial.

In the case of internal pressure tests, without external axial force applied ($F = 0$), the biaxiality ratio is equal to $\sigma_{zz}^{qb}/\sigma_{\theta\theta}^{qb} = 1/2$, leading to $\alpha = \sigma_{zz}/\sigma_{\theta\theta} = 0.47$.

Concerning the numerical simulations of internal pressure tests a biaxial stress state is applied $\sigma_{zz}/\sigma_{\theta\theta} = 1/2$. This gives the same response as a fully triaxial stress state with $\sigma_{zz}/\sigma_{\theta\theta} = 0.47$ since the model is only sensitive to the deviatoric stress tensor and since the deviatoric stress of a biaxial stress state with $\sigma_{zz}/\sigma_{\theta\theta} = 1/2$ is equal to deviatoric stress of the triaxial stress state with $\sigma_{zz}/\sigma_{\theta\theta} = 0.47$.

References

Andrade-Campos, A., Thuillier, S., Pilvin, P., Teixeira-Dias, F., 2007. On the determination of material parameters for internal variable thermoelastic–viscoplastic constitutive models. International Journal of Plasticity 23, 1349–1379.

Barbe, F., Decker, L., Jeulin, D., Cailletaud, G., 2001. Intergranular and intragranular behavior of polycrystalline aggregates. Part 1: F.E. model. International Journal of Plasticity 17, 513–536.

Barton, N. R., Arsenlis, A., & Marian, J. (2013). A polycrystal plasticity model of strain localization in irradiated iron. Journal of the Mechanics and Physics of Solids, 61(2), 341-351.

Berveiller, M., Zaoui, A., 1978. An extension of the self-consistent scheme to plastically-flowing polycrystals. Journal of the Mechanics and Physics of Solids 26, 325–344.

Bossis, P., Verhaeghe, B., Doriot, S., Gilbon, D., Chabretou, V., Dalmais, A., Mardon, J.-P., Blat, M., Miquet, A., 2009. In PWR Comprehensive Study of High Burn-Up Corrosion and Growth Behavior of M5® and Recrystallized Low-Tin Zircaloy-4. Zirconium in the Nuclear Industry: 15th International Symposium, ASTM International, ASTM STP 1505, 430–456.

Cailletaud, G., 1992. A micromechanical approach to inelastic behaviour of metals. International Journal of Plasticity 8, 55–73.

Cailletaud, G., Pilvin, P., 1994. Utilisation de modèles polycristallins pour le calcul par éléments finis. Revue Européenne des Éléments Finis 3, 515–541.

Capolungo, L., Beyerlein, I. J., Kaschner, G. C., & Tomé, C. N. (2009). On the interaction between slip dislocations and twins in HCP Zr. Materials Science and Engineering: A, 513, 42-51.

Carpenter, G.J.C., Northwood, D.O., 1975. The contribution of dislocation loops to radiation growth and creep of Zircaloy - 2. Journal of Nuclear Materials 56, 260–266.

Chakraborty, P., & Biner, S. B. (2016). Crystal plasticity modeling of irradiation effects on flow stress in pure-iron and iron-copper alloys. Mechanics of Materials, 101, 71-80.

Christodoulou, N., 1989. Evolution of the Bauschinger effect in tension and compression in Zircaloy-2. Acta Metallurgica 37, 529–539.

Delobelle, P., Robinet, P., Geyer, P., Bouffioux, P., 1996. A model to describe the anisotropic viscoplastic behaviour of Zircaloy-4 tubes. Journal of Nuclear Materials 238, 135–162.

Diard, O., Leclercq, S., Rousselier, G., Cailletaud, G., 2005. Evaluation of finite element based analysis of 3D multicrystalline aggregates plasticity. International Journal of Plasticity 21, 691–722.

Dickson, J. I., Boutin, J., Handfield, L., 1984. A comparison of two simple methods for measuring cyclic internal and effective stresses. Materials Science and Engineering, 64(1), L7-L11.

Doriot, S., Gilbon, D., Béchade, J.-L., Mathon, M.-H., Legras, L., Mardon, J.-P., 2005. Microstructural Stability of M5™ Alloy Irradiated up to High Neutron Fluences. Zirconium in the Nuclear Industry: Fourteenth International Symposium, ASTM International, ASTM STP 1467, 175-201.

Doriot, S., Verhaeghe, B., Béchade, J.-L., Menut, D., Gilbon, D., Mardon, J.-P., Cloué, J.-M., Miquet, A., Legras, L., 2014. Microstructural Evolution of M5 Alloy Irradiated in PWRs up to High Fluences—Comparison With Other Zr-Based Alloys. Zirconium in the Nuclear Industry: 17th Volume, ASTM International, ASTM STP 1543, 759–799.

Doriot, S., Verhaeghe, B., Soniak-Defresne, A., Bossis, P., Gilbon, D., Chabretou, V., Mardon, J.-P., Ton-That, M., Ambard, A., 2018. Microstructural Evolution of Q12TM Alloy Irradiated in PWRs and Comparison with Other Zr Base Alloys. Zirconium in the Nuclear Industry: 18th International Symposium, ASTM International, ASTM STP 1597, 823–856.

Drouet, J., Dupuy, L., Onimus, F., Mompiou, F., Perusin, S., Ambard, A., 2014. Dislocation dynamics simulations of interactions between gliding dislocations and radiation induced prismatic loops in zirconium. Journal of Nuclear Materials 449, 252–262.

Erinosho, T. O., & Dunne, F. P. E. (2015). Strain localization and failure in irradiated zircaloy with crystal plasticity. International Journal of Plasticity, 71, 170-194.

Evrard, P., Aubin, V., Pilvin, P., Degallaix, S., Kondo, D., 2008. Implementation and validation of a polycrystalline model for a bi-phased steel under non-proportional loading paths. Mechanics Research Communications 35, 336–343.

Feaugas, X., 1999. On the origin of the tensile flow stress in the stainless steel AISI 316L at 300 K: back stress and effective stress. Acta Materialia 47, 3617–3632.

Feaugas, X., Pilvin, P., Clavel, M., 1997. Cyclic deformation behaviour of an A/B titanium alloy—ii. Internal stresses and micromechanic modelling. Acta Materialia 45, 2703–2714.

Gélébart, L., & Mondon-Cancel, R. (2013). Non-linear extension of FFT-based methods accelerated by conjugate gradients to evaluate the mechanical behavior of composite materials. Computational Materials Science, 77, 430-439.

Gérard, C., Cailletaud, G., Bacroix, B., 2013. Modeling of latent hardening produced by complex loading paths in FCC alloys. International Journal of Plasticity 42, 194–212.

Hoc, T., Forest, S., 2001. Polycrystal modelling of IF-Ti steel under complex loading path. International Journal of Plasticity 17(1), 65-85

Hure, J., El Shawish, S., Cizelj, L., & Tanguy, B. (2016). Intergranular stress distributions in polycrystalline aggregates of irradiated stainless steel. Journal of Nuclear Materials, 476, 231-242.

Kassam, Z. H., & Wang, Z. (1993). Bauschinger effect in a modified Zr-2.5 wt.% Nb pressure tube material. Materials Science and Engineering: A, 171(1-2), 55-63.

Knezevic, M., Beyerlein, I. J., Brown, D. W., Sisneros, T. A., & Tomé, C. N. (2013). A polycrystal plasticity model for predicting mechanical response and texture evolution during strain-path changes: application to beryllium. International Journal of Plasticity, 49, 185-198.

Kocks, U.F., Tomé, C.N., Wenk, H.-R., 1998. Texture and anisotropy, preferred orientations in polycrystals and their effect on materials properties. Cambridge University Press, first edition.

MacEwen, S.R., Ells, C.E., Woo, O.T., 1981. The Bauschinger effect in Zircaloy-2. Journal of Nuclear Materials 101, 336–349.

Marano, A., Gélébart, L., Forest, S. (2019). Intragranular localization induced by softening crystal plasticity: Analysis of slip and kink bands localization modes from high resolution FFT-simulations results. Acta Materialia, 175, 262-275.

Méric, L., Cailletaud, G., Gaspérini, M., 1994. F.E. calculations of copper bicrystal specimens submitted to tension-compression tests. Acta Metallurgica et Materialia 42, 921–935.

Northwood, D.O., Rosinger, H.E., 1980. Influence of oxygen on the elastic properties of Zircaloy-4. Journal of Nuclear Materials 89, 147–154.

O'Donnell, W.J., Langer, B.F., 1964. Fatigue Design Basis for Zircaloy Components. Nuclear Science and Engineering 20, 1–12.

Onimus, F., Béchade, J.L., 2012. Radiation Effects in Zirconium Alloys. Comprehensive Nuclear Materials 1–31.

Onimus, F., Béchade, J.-L., 2009. A polycrystalline modeling of the mechanical behavior of neutron irradiated zirconium alloys. Journal of Nuclear Materials 384, 163–174.

Onimus, F., Béchade, J.L., Duguay, C., Gilbon, D., Pilvin, P., 2006. Investigation of neutron radiation effects on the mechanical behavior of recrystallized zirconium alloys. Journal of Nuclear Materials 358, 176–189.

Onimus, F., Béchade, J.L., Gilbon, D., 2012. Experimental Analysis of Slip Systems Activation in Neutron-Irradiated Zirconium Alloys and Comparison with Polycrystalline Model Simulations. Metallurgical and Materials Transactions A 44, 45–60.

Onimus, F., Bechade, J.-L., Prioul, C., Pilvin, P., Monnet, I., Doriot, S., Verhaeghe, B., Gilbon, D., Robert, L., Legras, L., Mardon, J.-P., 2005. Plastic Deformation of Irradiated Zirconium Alloys: TEM Investigations and Micro-Mechanical Modeling. Zirconium in the Nuclear Industry: Fourteenth International Symposium, ASTM International, ASTM STP 1467, 53-78.

Onimus, F., Bono, M., Garnier, J., Soniak-Defresne, A., Limon, R., Gilbon, D., Bourlier, F., Ambard, A., 2018. Strain-Path Change Tests and Physically Based Polycrystalline Modeling of the Behavior of Recrystallized Zirconium Alloys. Zirconium in the Nuclear Industry: 18th International Symposium, ASTM International, ASTM STP 1597, 180–213.

Onimus, F., Monnet, I., Béchade, J.., Prioul, C., Pilvin, P., 2004. A statistical TEM investigation of dislocation channeling mechanism in neutron irradiated zirconium alloys. Journal of Nuclear Materials 328, 165–179.

Pilvin, P. (2010). Notice d'utilisation de SiDoLo version 2.5. Institut de Recherche Dupuy de Lôme, Université de Bretagne-Sud.

Priser, M., Rautenberg, M., Cloué, J.-M., Pilvin, P., Feaugas, X., Poquillon, D., 2010. Multiscale Analysis of Viscoplastic Behavior of Recrystallized Zircaloy-4 at 400°C. Zirconium in the Nuclear Industry: 16th International Symposium, ASTM International, ASTM STP 1529, 269–297.

Proust, G., Tomé, C. N., Jain, A., & Agnew, S. R. (2009). Modeling the effect of twinning and detwinning during strain-path changes of magnesium alloy AZ31. International Journal of Plasticity, 25(5), 861-880.

Rousselier, G., Leclercq, S., 2006. A simplified "polycrystalline" model for viscoplastic and damage finite element analyses. International Journal of Plasticity 22, 685–712.

Schwenk, E.B., Wheeler, K.R., Shearer, G.D., Webster, R.T., 1978. Poisson's ratio in zircaloy-4 between 24° and 316°C. Journal of Nuclear Materials 73, 129–131.

Thomas, R., Lunt, D., Atkinson, M. D., da Fonseca, J. Q., Preuss, M., Barton, F., ... & Frankel, P. (2019). Characterisation of irradiation enhanced strain localisation in a zirconium alloy. Materialia, 5, 100248.

Vincent, L., 2008. On the ability of some cyclic plasticity models to predict the evolution of stored energy in a type 304L stainless steel submitted to high cycle fatigue. European Journal of Mechanics - A/Solids 27, 161–180.

Wisner, S., Reynolds, M., Adamson, R., 1994. Fatigue Behavior of Irradiated and Unirradiated Zircaloy and Zirconium. Zirconium in the Nuclear Industry: Tenth International Symposium, ASTM STP 1245, 499-499.

Xiao, X., Song, D., Xue, J., Chu, H., & Duan, H. (2015). A size-dependent tensorial plasticity model for FCC single crystal with irradiation. International Journal of Plasticity, 65, 152-167.

Xiao, X., Terentyev, D., Yu, L., Bakaev, A., Jin, Z., & Duan, H. (2016). Investigation of the thermo-mechanical behavior of neutron-irradiated Fe-Cr alloys by self-consistent plasticity theory. Journal of Nuclear Materials, 477, 123-133.